Publisher version: 10.1002/solr.202000771

Dopant-free bifacial silicon solar cells

Wenjie Lin, Julie Dréon, Sihua Zhong, Vincent Paratte, Luca Antognini, Jean Cattin, Zongtao Liu, Zongcun Liang, Pingqi Gao, Hui Shen, Christophe Ballif, and Mathieu Boccard*

W. Lin, Z. Liu, Prof. Z. Liang, Prof. H. Shen
Institute for Solar Energy Systems
School of Physics and State Key Laboratory of Optoelectronic Materials and Technologies
Sun Yat-Sen University (SYSU)
Guangzhou 510006, China
E-mail: shenhui1956@163.com

W. Lin, J. Dréon, V. Paratte, L. Antognini, Dr. J. Cattin, Prof. C. Ballif, and Dr. M. Boccard
Photovoltaics and Thin Film Electronics Laboratory
Institute of Microengineering
École Polytechnique Fédérale de Lausanne (EPFL)
Rue de la Maladière 71b, Neuchâtel CH-2000, Switzerland

Dr. S. Zhong
School of Science
Jiangsu Ocean University
Lianyungang, Jiangsu Province 222005, China

Prof. Z. Liang, Prof. H. Shen
Shunde-SYSU Institute for Solar Energy
Beijiao, Shunde 528300, China

Prof. P. Gao
School of Materials
Sun Yat-sen University
Guangzhou 510275, China

Prof. H. Shen
Jiangsu Collaborative Innovation Center of Photovoltaic Science and Engineering
Changzhou University
Changzhou 213164, Jiangsu Province, China

Keywords: silicon solar cell, dopant free, carrier selective contact, partial contact, bifacial solar cell

Abstract: This work discusses challenges to fabricate full-dopant-free bifacial silicon solar cells and demonstrates efficient devices utilizing MoO_3/ITO/Ag hole-selective contact and ZnO/LiF_x/Al electron-selective contacts with up to 79% short-circuit current bifaciality. The ZnO/LiF_x/Al rear electron contact features full-area ZnO anti-reflective coating and LiF_x/Al finger contact, allowing sunlight absorption from the back side, thus producing more overall

power. The ZnO/LiF_x/Al electron contacts with a thinner ZnO layer and a larger contact fraction display a better selectivity and a lower resistance loss. When considering rear-side irradiance of 0.15 sun, the dopant-free bifacial solar cell with 60 nm ZnO and 50%-LiF_x/Al metal contact fraction achieves a 3% estimated output power density improvement compared with its monofacial counterpart (21.0 mW/cm^2 compared to 20.3 mW/cm^2) using full area back contact. Both efficiency and bifaciality factor of this dopant-free device are still significantly lower than these of state-of-the-art devices relying on doped silicon-based layers, and we discuss the required improvement for this technology to become industry-relevant.

1. Introduction

Direct metallization on lightly doped silicon due to the Fermi-level pinning effect induced by a high density of bandgap states or defects, results in a relatively high Schottky barrier height, which leads to a very high rate of minority carrier recombination and a high contact resistance [1]. Dopant-free passivating contacts feature non-silicon materials with high or low work function and wide bandgap, combined with intrinsic hydrogenated amorphous silicon (a-Si: H(i)) or SiO_x passivating interlayer, depinning the Fermi-level and mitigating the density of defects and Schottky barrier height [2,3]. Such contact technique has the potential to provide excellent passivation (quantified by a low value of dark saturation current density, J_0) and low contact resistivity (ρ_c) using simple and inexpensive fabrication methods. Therefore, extensive efforts have been devoted to the improvement of silicon solar cells with dopant-free passivating contacts [4-9]. By replacing a-Si:H(p) with a 4-nm-thick hole-collecting and transparent molybdenum oxide (MoO_x) layer, a remarkable solar-cell efficiency of 23.5% was recently demonstrated [10]. The integration of a-Si:H(i)/LiF_x/Al electron selective contact at the rear side, instead of a-Si:H(i)/ a-Si:H(n)/ITO/Ag [11], enabled the development of a fully dopant-free silicon solar cells without any doped a-Si:H layers or diffused p-n junctions. The further insertion of thick ZnO interlayer (75 nm) between a-Si:H(i) and LiF_x mitigated plasmonic

absorption on the back side, achieving an efficiency of 21.4% [12]. Moreover, by introducing interdigitated back contact (IBC) cell structure, fully dopant-free multilayer back-contact solar cells reached the record efficiency of 22.1% in this category [13].

However, the efficiency of the best fully dopant-free IBC solar cells is still much lower than the device utilizing Si-based contacts [14-16]. Moreover, the complex and expensive patterning need has so far hindered the widespread industrialization of IBC technologies. Hence, recent tremendous attention has been paid to bifacial silicon solar cells and modules, attributed to an increase in the energy output of photovoltaic systems compared with monofacial operation, which therefore decreases levelized cost of electricity [17-19]. Dopant-free bifacial silicon solar cells haven't been reported in literature yet. This is due to the need for a thick-enough Al layer to provide the electron-selectivity of dopant-free electron-transporting stacks [9,12,13,20-26]. A notable exception is the recently reported device employing a single TiN layer as electron-selective contact, yet this material is opaque due to high free-carrier density [27].

To fabricate transparent electron-selective contacts, several approaches can be envisioned, either by combining low-work-function materials with transparent conductive oxides (preferentially with low work-function such as ZnO) [11,12] or by using ultra-thin films of low-work-function metal (possibly embedded in an oxide-metal-oxide structure) [28,29]. Table 1 gives a representative overview of the numerous bifacial silicon heterojunction solar cells we fabricated and tested. The cells feature a-Si:H (i)/a-Si:H (p)/ITO/Ag front hole contact and various optimized transparent electron materials capped with full-area ITO/Ag grid, full-area AZO/Ag grid, or simple Ag grid. All of them display poor device performance, except the standard silicon heterojunction bifacial solar cells using a-Si: H(n) as the electron-selective material.

One approach to realize dopant-free bifacial silicon solar cells consists in using partial area electron-selective contacts [2,7,8,19,25]. In the work developed by Zhong et al., the a-Si: H(i)/ZnO/LiF_x/Al contact exhibited a J_0 of 3.5 fA/cm^2 and ρ_c of 0.136 Ω·cm^2 [12,30]. In that

case, the contact resistance is potentially low to form partial area heterocontact for dopant-free bifacial silicon solar cells with a metal contact fraction between 10%-50% [31]. Contrary to most of electron transporting layers (0.5-10 nm) [6,9,13,20-24,27,32-34], thick ZnO (60~140 nm) electron selective layer can additionally serve as transparent anti-reflective coating (ARC), thus simplifying the fabrication process.

In this contribution, we have developed full dopant-free bifacial silicon solar cells for the first time, featuring both MoO_3/ITO/Ag hole-selective contact and ZnO/LiF_x/Al electron-selective contacts. The ZnO/LiF_x/Al rear electron contacts consist of full-area ZnO ARC and grid-shaped LiF_x/Al contact. We have also evidenced the importance of the metal contact fraction of LiF_x/Al and the thickness of ZnO on back side to optimize the front and rear output power generation.

2. Results and discussion

2.1. Fabrication process

Dopant-free bifacial solar cells were fabricated on n-type float zone c-Si wafers with a thickness of ~ 195 μm and resistivity of ~ 2.1 Ω cm, as shown in Figure 1. After etching, alkaline texturing, cleaning by the Radio Corporation of American procedure, and dipping in hydrofluoric acid (5%) leaving a pristine H-terminated surface [35], a-Si:H(i) layers (~ 9 nm) were deposited on both sides by a plasma-enhanced chemical vapor deposition (PECVD), which suppress the Fermi-level pinning effect and reduce the density of defects, providing excellent passivation. Thermal evaporation of MoO_3 (~ 5 nm on textured surface) was conducted on front surface, followed by magnetron sputtering of indium tin oxide (ITO, ~ 75 nm) using a mask to generate cells with an area of 2 cm × 2 cm. Subsequently, low-pressure chemical vapor deposited (LPCVD) ZnO films with the various thicknesses (d_{ZnO}, 60–180 nm) were grown on rear side, prior to annealing at 150 °C. The reported values for d_{ZnO} were obtained using ellipsometry measurements on polished wafers, which are similar to the

thickness on textured wafers based on their color. Then, the front side of the devices was screen printed to create the Ag grids (Finger width of ~40 µm and pitch of 1.85 mm with external busbars) and cured at 130 °C. Finally, on the back side, series of masks were applied to define various metal contact fraction (16.7%, 33.3%, 50%, 66.7%, 100%, the corresponding pitch width are 300 µm, 600 µm, 900 µm, 1200 µm, full area, the pitch length is 2 cm), during LiF_x (1.5 nm)/Al (200 nm) evaporation, to enable bifaciality. The use of high-work-function MoO_x/ITO/Ag contact and low-work-function ZnO/LiF_x/Al contact induces the asymmetrical band-bending on both surfaces, achieving the asymmetrical carrier selective contacts. In the latter case, the use of LiF_x/Al is crucial to reach a low contact resistance [12]. Also the LPCVD ZnO layers have a sheet resistance of $5.3 \times 10^7 \sim 1.2 \times 10^8$ Ω/□ [12], which is too high to contribute significantly to lateral carrier transport. Therefore, only the n-Si substrate (108 Ω/□) provides the lateral carrier transport towards LiF_x/Al fingers for bifacial devices.

For the cells with the area of 1.1 cm^2 shown in Table 1, a-Si:H(p) and a-Si:H(n) layers were deposited by PECVD. The AZO films were sputtered using AZO (Al_2O_3: 2 wt%) with O_2/(Ar + O_2) flow ratio of 0 and 0.35% at room temperature. The TiN films were deposited by reactive magnetron sputtering using a pure titanium target with N_2/(Ar + N_2) flow ratio of 0 ~ 28.6% at room temperature. The ZnS (12 nm)/Mg (10 nm)/ZnS (60 nm) stack was evaporated using pure ZnS and Mg particle sources at room temperature. Back Ag grids were sputtered via the metal mask.

Light *J-V* characteristics of dopant-free bifacial solar cells were measured with illumination from either the front or the rear side using a Wacom WXS-90S-L2 solar simulator, under standard test condition (STC, AM 1.5G, 100 mW/cm^2, and 25 °C). External quantum efficiency (EQE) spectra and reflectance were characterized utilizing an in-house built setup and spectrophotometer (Lambda-950, Perkin Elmer), respectively, in the non-metalized area.

2.2. Device performance

Figure 2 displays the effect of ZnO thickness and LiF_x/Al metal contact fraction on the front-side-illuminated cell parameters and the rear-side-illuminated J_{SC}^r at an illumination of 1 Sun, respectively. As shown in Figure 2a, the reduction of LiF_x/Al metal contact fraction decreases slightly the open circuit voltage (V_{OC}^f) measured with front-side illumination. When thinning the ZnO layers, the V_{OC}^f is higher.

As displayed in Figure 2b, all the cells show relatively low front-side-illuminated *FF* values (FF^f), even the cells with full area back contact (< 74%, compared to the 77.3% reported in [12]). Fitting of these *J-V* curves evidenced a relatively low p*FF* around 82%, and a relatively high series resistance around 1.5 Ohm.cm^2. These modest values are possibly due to our process variability, or to an already mild degradation between the fabrication and measurement (even though waiting time was minimized [30]). Efficiencies around 20.5% are nevertheless reached for the two thinnest ZnO films (Fig. 2d).

Then, when using partial-area LiF_x/Al, FF^f drops to as low as 63% for the thickest ZnO film or 69% for the thickest one. Indeed, restricting the rear metal contact fraction increases series resistance due to the rear contact resistance ($R_{S,contact} \approx \rho_c$/metal contact fraction) and the lateral resistance in n-Si subtract ($R_{S,lateral}$) [36]. Note that conversely, since the whole rear side was in contact with the metallic measurement chuck, $R_{S,finger}$ is not expected to contribute to $R_{S,total}$ (similarly to a "busbarless" measurement) for any finger width. The increase in series resistance is obvious in Fig. 3a, and Fig. 3b shows which the series resistance extracted from two-diode fits of the data, confirming this interpretation.

We performed simulations using the framework developed in Ref. [36] to quantitatively evaluate how the different rear metallization patterns affect $R_{S,contact}$, and $R_{S,lateral}$ for different values of contact resistance from 0.1 Ω·cm^2 to 0.4 Ω·cm^2. The range of variation is represented in Fig. 3 as the orange areas. Among them, the $R_{S,contact}$ presents the most significant contribution to the variation upon narrowing the rear metal fingers. By comparing these

simulation results to our experimental data, a reasonable agreement can be obtained for a contact resistance of 0.2 Ohm.cm^2 for the 60-nm-ZnO case, and up to 0.4 Ohm.cm^2 for the 140-nm one. For all cases, an identical lump value of 1.3 Ohm.cm^2 was used for the contribution to series resistance from the front contact stack and front grid ($R_{S,rest}$).

The trends of V_{OC}^{f} and FF^{f} indicate thus that thinner ZnO and higher metal contact fraction provide better selectivity and lower resistance loss [31,37]. However, Figure 2c suggests neither significant impact from metal contact fraction nor d_{ZnO} on the J_{SC}^{f} illuminated from the front-side, but as expected a strong linear influence of the contact-area fraction on the J_{SC}^{r} (measured with rear-side illumination). Finally, the change of the power conversion efficiency (PCE^{f}) obtained with front-side illumination is essentially consistent with the trends of V_{OC}^{f} and FF^{f}.

2.3. Estimated output power density

The challenge for the widespread adoption of bifacial photovoltaic technology is the standardization of characterization and simulation [38]. The bifacial solar cells absorb photons from both sides simultaneously, behaving differently with the cells receiving sunlight from one side only. The International Electrotechnical Commission published the IEC 60904 series, which describe the requirements for indoor measurement of solar cells and modules under STC, and for outdoor performance assessment [39]. A bifacial solar cell can be regarded as a monofacial solar cell, whose operating current is equal to the sum of the currents generated on both sides of the bifacial solar cell. Here, we assume that the short circuit current (J_{SC}) of a bifacial solar cell varies linearly with illumination density and is equal to the sum of the front- and rear-side-illuminated J_{SC} [38]. To estimate the total energy output of dopant-free bifacial solar cells, the effective output power density (P_{out}^{b}) is given by [40]

$$P_{out}^{b} = \left(J_{SC}^{f} + \frac{P_i^{r}}{P_i^{f}} J_{SC}^{r}\right) \times V_{OC}^{b} \times FF^{b} \quad (1)$$

Where P_i^f and P_i^r correspond to the power densities of the illumination source on the front-side and rear-side respectively, V_{OC}^b and FF^b are effective V_{OC} and FF of a bifacial solar cell. Here, P_i^f is defined to be 100 mW/cm^2, according to standard test conditions. For realistic bifacial application, we chose P_i^r to be 15 mW/cm^2, which is in between the 10% and 20% described in regulatory documents [39]. To account for the increased generation rate due to bifacial illumination, the following equations are given to calculate V_{OC}^b and FF^b [40]:

$$V_{\mathrm{OC}}^b = V_{\mathrm{OC}}^f \times \frac{\ln\left(\left(J_{\mathrm{SC}}^f + \frac{P_i^r}{P_i^f} J_{\mathrm{SC}}^r\right) \Big/ J_0\right)}{\ln\left(J_{\mathrm{SC}}^f \Big/ J_0\right)} \tag{2}$$

where J_0 is given by

$$J_0 = \frac{J_{\mathrm{SC}}^f}{\mathrm{e}^{(V_{\mathrm{OC}}^N)}} \tag{3}$$

Here, $V_{\mathrm{OC}}^N = V_{\mathrm{OC}}^f \frac{q}{nkT}$, where q is the electron charge, k is the Boltzmann constant, T is the temperature, n = 1 is diode quality factor.

FF^b can be written as

$$FF^b = FF^f \times \left(1 + \frac{J_{\mathrm{SC}}^r P_i^r}{J_{\mathrm{SC}}^f P_i^f} - \frac{J_{\mathrm{SC}}^r P_i^r pFF}{J_{\mathrm{SC}}^f P_i^f FF^f}\right) \tag{4}$$

Where pFF is the FF of the cell considering no resistive losses and is obtained from two-diode fits of our experimental data.

$$pFF = \frac{V_{\mathrm{OC}}^N - \ln(V_{\mathrm{OC}}^N - 0.72)}{V_{\mathrm{OC}}^N + 1} \tag{5}$$

As displayed in Figure 4, estimated P_{out}^b of dopant-free bifacial solar cells is calculated with various d_{ZnO} and LiF_x/Al contact area fraction. Compared with the cells featuring full LiF_x/Al back contact, the dopant-free bifacial solar cells using 100 nm and 140 nm exhibit lower P_{out}^b. However, as summarized in Table 2, the dopant-free bifacial solar cells with 60 nm ZnO

demonstrate improved P_{out}^{b} comparing to its monofacial counterpart (P_{out}^{b}=20.3 mW/cm^2). Finally, the optimized bifacial structure with 60 nm ZnO and the LiF_x/Al metal contact fraction of 50% results in the estimated P_{out}^{b} of 21.0 mW/cm^2. The P_{out}^{b} again of 0.7 mW/cm^2 (thus a 3% relative increase) is attributed to the good selectivity and low series resistance of thinner ZnO for partial contact and the balance of front and rear output power.

2.4. Optical analysis

In order to further understand the effect of d_{ZnO} on the front and back optical characteristics, Figure 5 shows the optical analysis of dopant-free bifacial solar cells using a-Si:H (i)/ZnO/LiF_x/Al contacts with the metal contact fraction of 50%. Figure 5a suggests that varying d_{ZnO} exhibits no impact on the J_{SC}^{f}, consistent with similar front side EQE and reflectance (Figure 5b). This result comes in agreement with the previous J_{SC}^{f} analysis. However, the variation of d_{ZnO} affects the J_{SC}^{r} significantly, due to the function of ARC on back side [42]. The dopant-free bifacial solar cells with d_{ZnO} of 100 nm demonstrate the best J_{SC}^{r} and EQE illuminated from the rear side, attributed to the rear lowest reflectance at 600 nm, shown in Figure 5c. Yet, thanks to better selectivity and lower resistance loss leading to higher V_{OC}^{f} and FF^{f}, the 60 nm ZnO layer is optimal for bifacial solar cell performance and yields the highest estimated P_{out}^{b} in our study. A finer thickness study around 60 nm (e.g. between 40 nm and 80 nm) could potentially enable slightly higher efficiencies, but the marginal differences only are expected due to the degradation of electrical performance upon thickening and of optical performance upon thinning down the ZnO layer.

Finally, to put these results in perspective with best-in-class bifacial devices, both efficiency (~20%) and bifaciality factor for this device (~50%) are still largely inferior to typical values for standard bifacial devices using doped silicon as contacts (typically up to 24% efficiency and 95% bifaciality). As discussed in the introduction, this is due to the non-alleviated need for an opaque Al layer to provide electron-selectivity to the contact stack, and

to the still relatively high contact resistance value for this contact stack compared to best-in-class ones relying on doped silicon. In addition, the degradation of ZnO/LiF_x/Al contacts is caused by the deteriorated work function of LiF_x/Al due to the interaction with Air [30]. The best bifacial solar cell exists an 8.2% PCE^f degradation after 6 h, due to partial contacts with more edge exposed in air. Significant progress, probably through the use of innovative materials, is still required for full-dopant-free bifacial solar cells to become a relevant technology.

Conclusion

In this contribution, we discussed the challenges of fabricating transparent dopant-free electron-selective contacts, and reported the first full dopant-free bifacial solar cells featuring MoO_3/ITO/Ag hole contact and ZnO/LiF_x/Al electron contact. The electron contacts are composed of full-area ZnO ARC and grid-shaped LiF_x/Al contact, enabling bifacial operation. The 60 nm ZnO is used to enhance selectivity and reduce resistance loss for partial rear contact. Finally, with a realistic 15% illumination from the rear-side, the best bifacial solar cell presented here with LiF_x/Al metal contact fraction of 50% can potentially grant a 0.7 mW/cm^2 estimated power output increase compared with the monofacial solar cells using full-area rear contact.

Acknowledgments

The authors thank Vincent Paratte for performing part of the wafer preparation and all group members in PV-lab EPFL. Funding from Swiss national science foundation under Ambizione Energy grant ICONS (PZENP2_173627) is also acknowledged. Wenjie Lin thanks for the financial support from China Scholarship Council (CSC, 201906380038). This work was partly supported by the National Natural Science Foundation of China (Grant Nos. 61774173, 61974169, 62034009 and 61774171), the Guangzhou Collaborative Innovation Major Project of producing, teaching and researching (Grant No. 201508010011), the Jiangsu Collaborative Innovation Center of Photovoltaic Science and Engineering (Grant No.

SCZ1405500002), the Natural Science Foundation for Distinguished Young Scholars of Guangdong Province (Grant No. 2019B151502053).

Conflict of Interest

The authors declare no conflict of interest.

Received:
Revised:
Published online:

References

[1] R.T. Tung, Appl. Phys. Rev., 1 (2014) 011304.

[2] T.G. Allen, J. Bullock, X. Yang, A. Javey, S. De Wolf, Nat. Energy, (2019) 1-15.

[3] J. Melskens, B.W. van de Loo, B. Macco, L.E. Black, S. Smit, W. Kessels, IEEE J. Photovoltaics, 8 (2018) 373-388.

[4] X. Yang, H. Xu, W. Liu, Q. Bi, L. Xu, J. Kang, M.N. Hedhili, B. Sun, X. Zhang, S. De Wolf, Adv. Electron. Mater., 6 (2020) 2000467.

[5] S. Cao, J. Li, J. Zhang, Y. Lin, L. Lu, J. Wang, M. Yin, L. Yang, X. Chen, D. Li, Adv. Funct. Mater., (2020) 2004367.

[6] X. Yang, Y. Lin, J. Liu, W. Liu, Q. Bi, X. Song, J. Kang, F. Xu, L. Xu, M.N. Hedhili, Adv. Mater., 32 (2020) 2002608.

[7] W. Lin, W. Wu, Q. Xie, Z. Liu, K. Qiu, L. Cai, Z. Yao, L. Meng, B. Ai, Z. Liang, ACS Appl. Mater. Interfaces, 10 (2018) 43699-43706.

[8] W. Lin, W. Wu, Z. Liu, K. Qiu, L. Cai, Z. Yao, B. Ai, Z. Liang, H. Shen, ACS Appl. Mater. Interfaces, 10 (2018) 13645-13651.

[9] J. Bullock, Y. Wan, Z. Xu, S. Essig, M. Hettick, H. Wang, W. Ji, M. Boccard, A. Cuevas, C. Ballif, ACS Energy Lett., 3 (2018) 508-513.

[10] J. Dréon, Q. Jeangros, J. Cattin, J. Haschke, L. Antognini, C. Ballif, M. Boccard, Nano Energy, (2020) 104495.

[11] J. Bullock, M. Hettick, J. Geissbühler, A.J. Ong, T. Allen, C.M. Sutter-Fella, T. Chen, H. Ota, E.W. Schaler, S. De Wolf, Nat. Energy, 1 (2016) 1-7.

[12] S. Zhong, J. Dreon, Q. Jeangros, E. Aydin, S. De Wolf, F. Fu, M. Boccard, C. Ballif, Adv. Funct. Mater., (2019) 1907840.

[13] W. Wu, W. Lin, S. Zhong, B. Paviet-Salomon, M. Despeisse, Q. Jeangros, Z. Liang, M. Boccard, H. Shen, C. Ballif, physica status solidi (RRL)–Rapid Research Letters, (2020).

[14] F. Haase, C. Hollemann, S. Schaefer, A. Merkle, M. Rienaecker, J. Krügener, R. Brendel, R. Peibst, Sol. Energy Mater. Sol. Cells, 186 (2018) 184-193.

[15] K. Yoshikawa, W. Yoshida, T. Irie, H. Kawasaki, K. Konishi, H. Ishibashi, T. Asatani, D. Adachi, M. Kanematsu, H. Uzu, Sol. Energy Mater. Sol. Cells, 173 (2017) 37-42.

[16] M.A. Green, K. Emery, Y. Hishikawa, W. Warta, E.D. Dunlop, Prog. Photovoltaics Res. Appl., 24 (2016) 3-11.

[17] T. Dullweber, C. Kranz, R. Peibst, U. Baumann, H. Hannebauer, A. Fülle, S. Steckemetz, T. Weber, M. Kutzer, M. Müller, Prog. Photovoltaics Res. Appl., 24 (2016) 1487-1498.

[18] F. Fertig, S. Nold, N. Wöhrle, J. Greulich, I. Hädrich, K. Krauß, M. Mittag, D. Biro, S. Rein, R. Preu, Prog. Photovoltaics Res. Appl., 24 (2016) 800-817.

[19] Y. Chen, D. Chen, C. Liu, Z. Wang, Y. Zou, Y. He, Y. Wang, L. Yuan, J. Gong, W. Lin, Prog. Photovoltaics Res. Appl., 27 (2019) 827-834.

[20] C. Reichel, U. Würfel, K. Winkler, H.-F. Schleiermacher, M. Kohlstädt, M. Unmüssig, C.A. Messmer, M. Hermle, S.W. Glunz, J. Appl. Phys., 123 (2018) 024505.

[21] M. Boccard, X. Yang, K. Weber, Z.C. Holman, Passivation and carrier selectivity of TiO 2 contacts combined with different passivation layers and electrodes for silicon solar cells, in: 2016 IEEE 43rd Photovoltaic Specialists Conference (PVSC), IEEE, 2016, pp. 2403-2407.

[22] W. Wang, J. He, L. Cai, Z. Wang, S.K. Karuturi, P. Gao, W. Shen, Solar RRL, (2020) 2000569.

[23] S.-H. Kim, J.-Y. Jung, R.B. Wehrspohn, J.-H. Lee, ACS Applied Energy Materials, 3 (2020) 3180-3185.

[24] J. Yu, M. Liao, D. Yan, Y. Wan, H. Lin, Z. Wang, P. Gao, Y. Zeng, B. Yan, J. Ye, Nano Energy, 62 (2019) 181-188.

[25] J. Bullock, Y. Wan, M. Hettick, X. Zhaoran, S.P. Phang, D. Yan, H. Wang, W. Ji, C. Samundsett, Z. Hameiri, Adv. Energy Mater., 9 (2019) 1803367.

[26] X. Yang, K. Weber, Z. Hameiri, S. De Wolf, Prog. Photovoltaics Res. Appl., 25 (2017) 896-904.

[27] X. Yang, W. Liu, M. De Bastiani, T. Allen, J. Kang, H. Xu, E. Aydin, L. Xu, Q. Bi, H. Dang, E. AlHabshi, K. Kotsovos, A. AlSaggaf, I. Gereige, Y. Wan, J. Peng, C. Samundsett, A. Cuevas, S. De Wolf, Joule, 3 (2019) 1314-1327.

[28] W. Wu, W. Lin, J. Bao, Z. Liu, B. Liu, K. Qiu, Y. Chen, H. Shen, RSC Adv., 7 (2017) 23851-23858.

[29] W. Wu, J. Bao, Z. Liu, W. Lin, X. Yu, L. Cai, B. Liu, J. Song, H. Shen, Mater. Lett., 189 (2017) 86-88.

[30] W. Lin, M. Boccard, S. Zhong, V. Paratte, Q. Jeangros, L. Antognini, J. Dréon, J. Cattin, J. Thomet, Z. Liu, ACS Applied Nano Materials, (2020).

[31] A. Cuevas, Y. Wan, D. Yan, C. Samundsett, T. Allen, X. Zhang, J. Cui, J. Bullock, Sol. Energy Mater. Sol. Cells, 184 (2018) 38-47.

[32] J. Cho, J. Melskens, M.R. Payo, M. Debucquoy, H.S. Radhakrishnan, I. Gordon, J. Szlufcik, W. Kessels, J. Poortmans, ACS Applied Energy Materials, 2 (2019) 1393-1404.

[33] X. Yang, E. Aydin, H. Xu, J. Kang, M. Hedhili, W. Liu, Y. Wan, J. Peng, C. Samundsett, A. Cuevas, Adv. Energy Mater., 8 (2018) 1800608.

[34] G. Masmitjà, P. Ortega, J. Puigdollers, L. Gerling, I. Martín, C. Voz, R. Alcubilla, J. Mater. Chem., 6 (2018) 3977-3985.

[35] P. Brabant, J. Ferrara, B. Pagliaro, K. Weeks, M. Rittgers, R. Scott, Y. Zhang, T. Landin, T. Irving, J. Spear, Appl. Surf. Sci., 255 (2008) 1741-1743.

[36] J. Haschke, G. Christmann, C. Messmer, M. Bivour, M. Boccard, C. Ballif, J. Appl. Phys., 127 (2020) 114501.

[37] R. Brendel, R. Peibst, IEEE J. Photovoltaics, 6 (2016) 1413-1420.

[38] T.S. Liang, M. Pravettoni, C. Deline, J.S. Stein, R. Kopecek, J.P. Singh, W. Luo, Y. Wang, A.G. Aberle, Y.S. Khoo, Energy Environ. Sci., 12 (2019) 116-148.

[39] V. Fakhfouri, IEC TS, (2019) 60904-60901.

[40] J.P. Singh, T.M. Walsh, A.G. Aberle, Prog. Photovoltaics Res. Appl., 22 (2014) 903-909.

[41] M.A. Green, Solid State Electron., 24 (1981) 788-789.

[42] A. Cruz, E.-C. Wang, A.B. Morales-Vilches, D. Meza, S. Neubert, B. Szyszka, R. Schlatmann, B. Stannowski, Sol. Energy Mater. Sol. Cells, 195 (2019) 339-345.

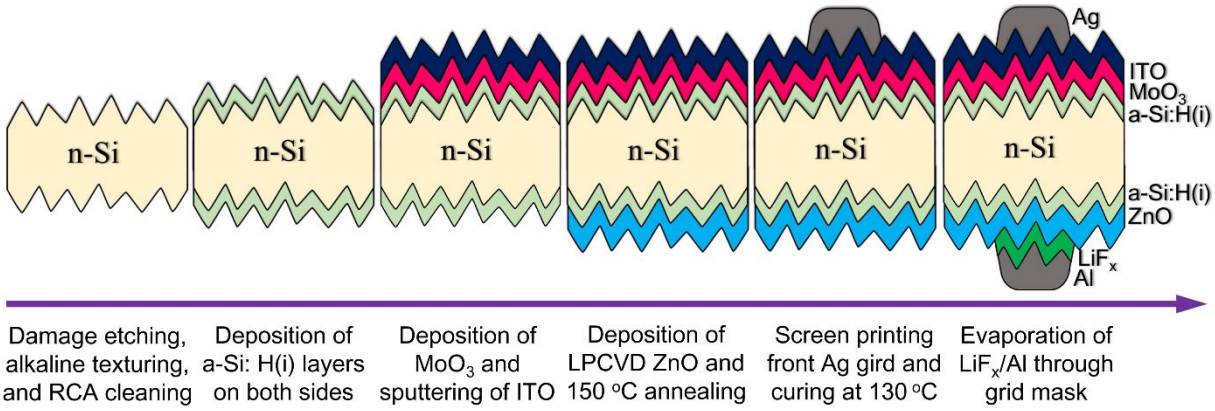

Figure 1. Fabrication steps of dopant-free bifacial solar cells featuring a-Si:H (i)/MoO_x/ITO/Ag hole contact and a-Si:H (i)/ZnO/LiF_x/Al electron contact.

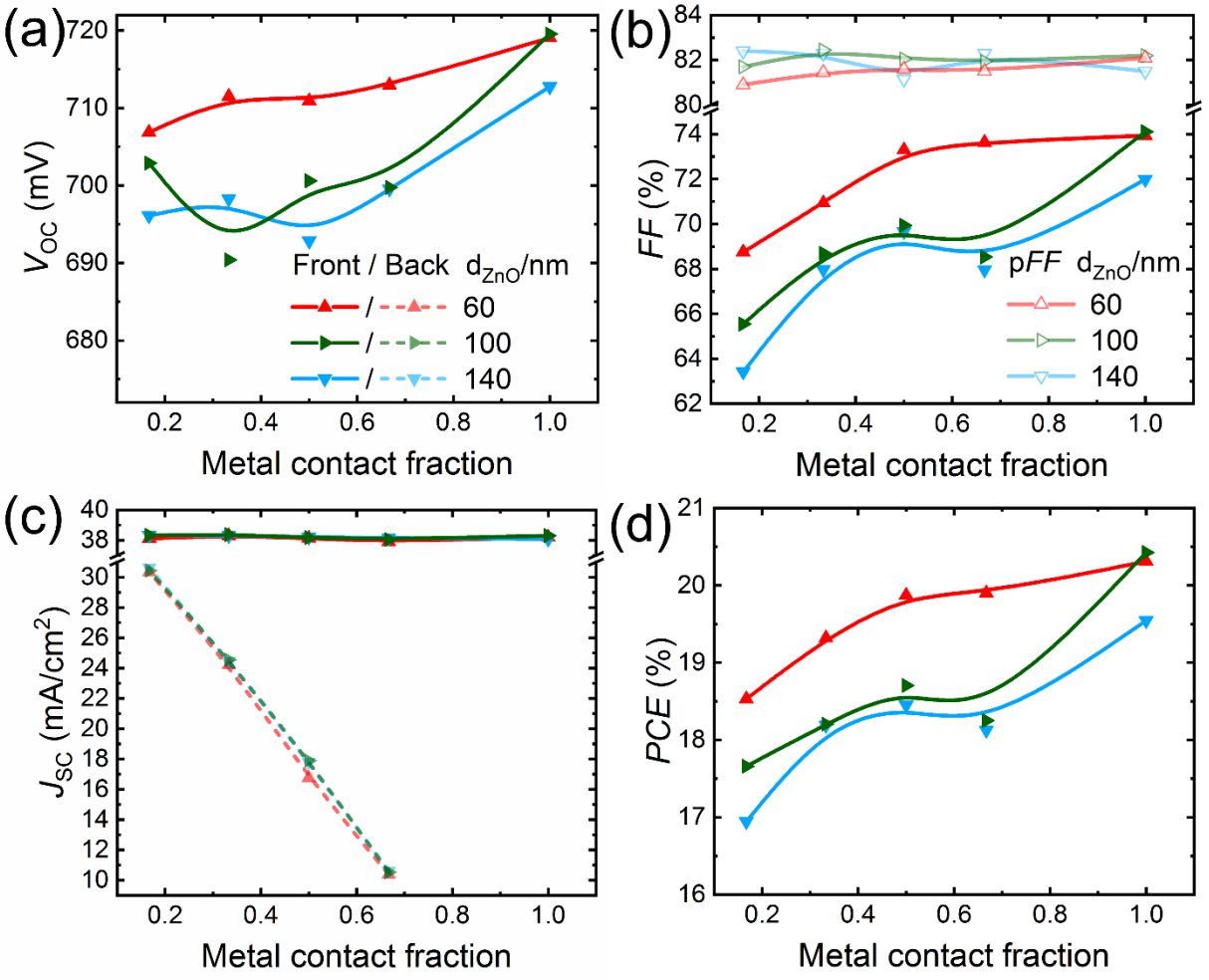

Figure 2. Device results of dopant-free bifacial solar cells. (a) V_{OC}, (b) p*FF* and *FF*, (c) J_{SC}, and (d) efficiency as a function of ZnO thickness and LiF_x/Al metal contact fraction, under front and rear side illumination.

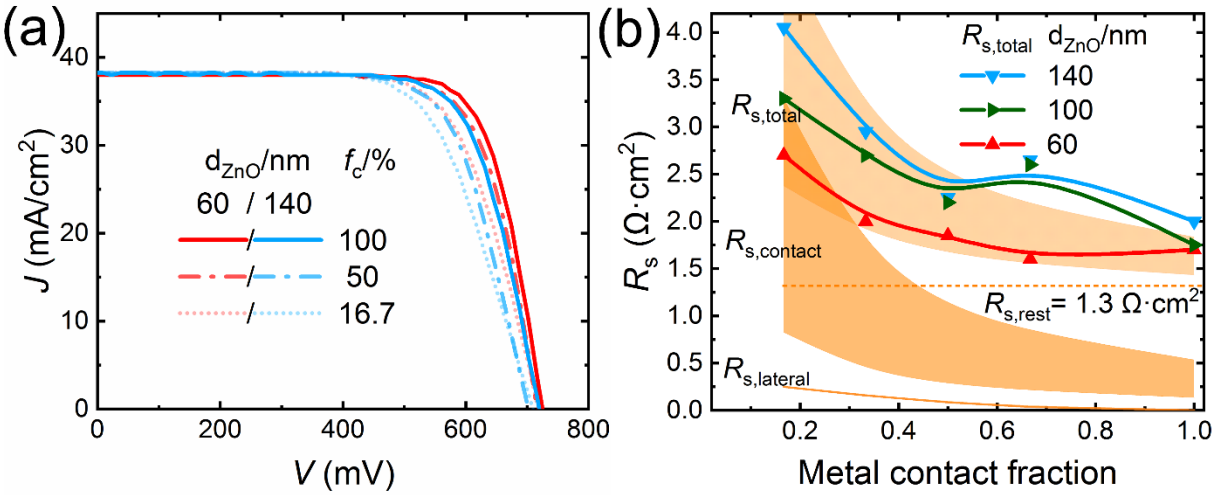

Figure 3. The *J*-*V* curve and the R_S analysis of dopant-free bifacial solar cells as a function of ZnO thickness and LiF_x/Al metal contact fraction (f_c).

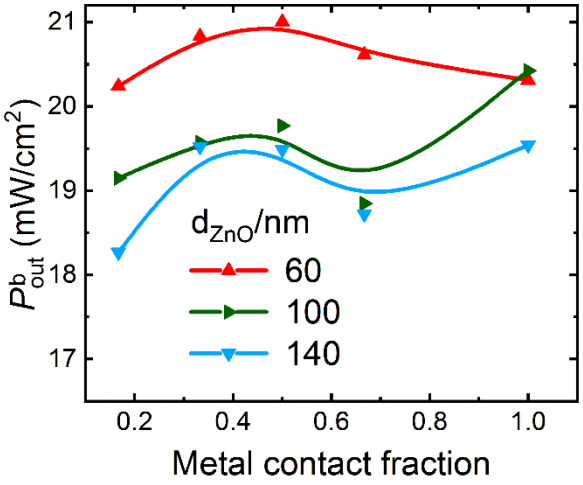

Figure 4. Estimated output power density of dopant-free bifacial solar cells, as a function of ZnO thickness and LiF_x/Al metal contact fraction.

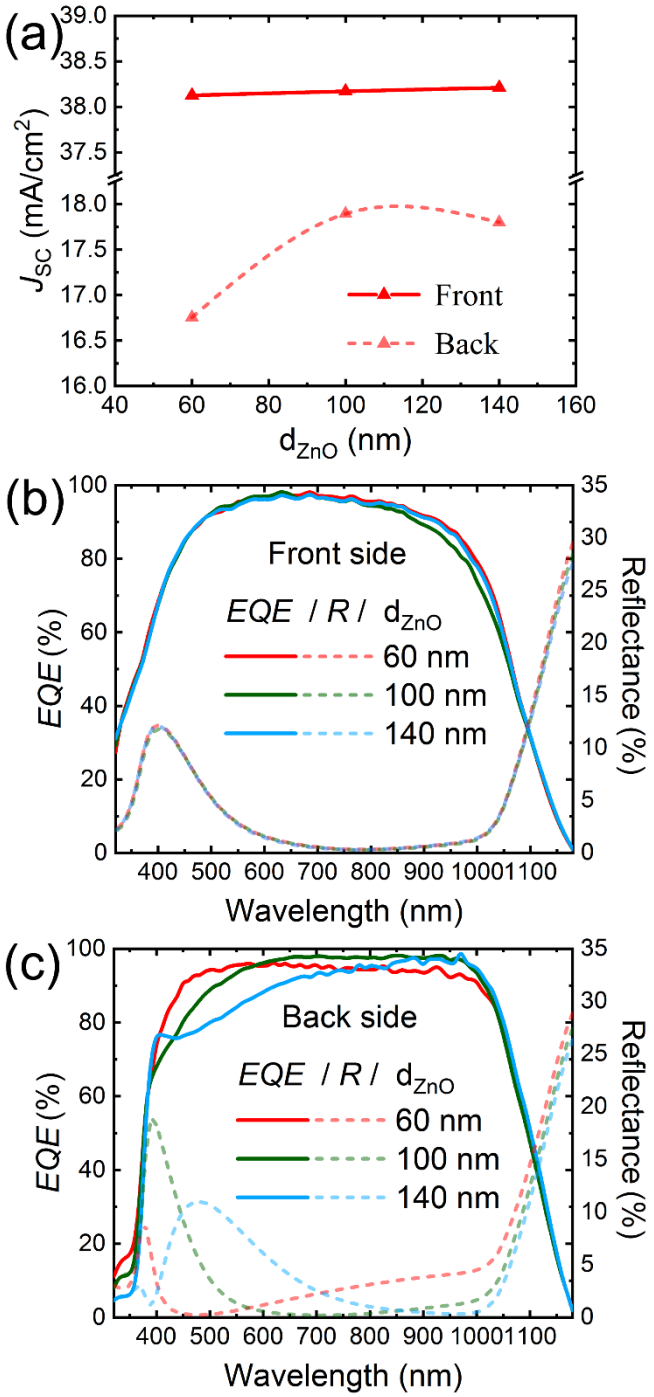

Figure 5. Optical analysis of dopant-free bifacial solar cells using a-Si:H (i)/ZnO/LiF_x/Al contacts with the back metal contact fraction of 50%, as function of ZnO thickness. (a) J_{SC}. EQE and reflectance under (b) front and (c) rear side illumination.

Table 1. Cell parameters of silicon heterojunction bifacial solar cells with a-Si:H (i)/a-Si:H (p)/ITO/Ag hole contact and various optimized transparent electron contacts.

Electron contact structure	*PCE* [%]	V_{OC} [mV]	J_{SC} [mA/cm^2]	*FF* [%]
a-Si: H(i)/a-Si: H(n)/ITO (75 nm)/Ag grid (Reference)	17.6	702.1	34.3	73.2
a-Si: H(i)/ZnO (100 nm)/ITO (75 nm)/Ag grid	0.10	346	1.7	17.1
a-Si: H(i)/ZnO (100 nm)/LiF_x (1.5 nm)/ITO (75 nm)/Ag grid	0.27	321.8	5.0	16.8
a-Si: H(i)/ZnO (100 nm)/LiF_x (1.5 nm)/Al (4 nm)/ITO (75 nm)/Ag grid	2.7	337.4	28.2	28.3
a-Si: H(i)/AZO (2 nm)/Al (12 nm)/AZO (60 nm)/Ag grid	9.6	498.0	29.6	65.3
a-Si: H(i)/ZnO (10 nm)/Al (12 nm)/AZO (60 nm)/Ag grid	10.8	526.2	31.1	65.8
a-Si: H(i)/TiN_x (80 nm)/Ag grid	7.7	410.0	29.8	62.8
a-Si: H(i)/TiN_x (10 nm)/AZO (80 nm)/Ag grid	9.7	485.6	29.5	67.8
a-Si: H(i)/ZnS (12 nm)/Mg (10 nm)/ZnS (60 nm)/Ag grid	0.39	526.9	4.6	16.3

Table2. Device parameters and estimated P_{out}^{b} of dopant-free monofacial and bifacial solar cells with a-Si:H (i)/ MoO_x/ITO/Ag hole contact and a-Si:H (i)/ZnO/LiF_x/Al electron contact featuring 60 nm ZnO and the LiF_x/Al metal contact fraction of 100% and 50%, respectively.

Metal contact fraction	illumination	P_{out}^{b} [mW/cm^2]	V_{OC} [mV]	J_{SC} [mA/cm^2]	*FF* [%]
100%	Front side	20.3	719.1	38.2	73.9
50%	Front side	19.9	710.9	38.1	73.3
	Rear side			16.8	
	Bifacial operation	21.0	712.6	40.6	72.5

Publisher version: 10.1002/solr.202000771

Dopant-free bifacial silicon solar cells

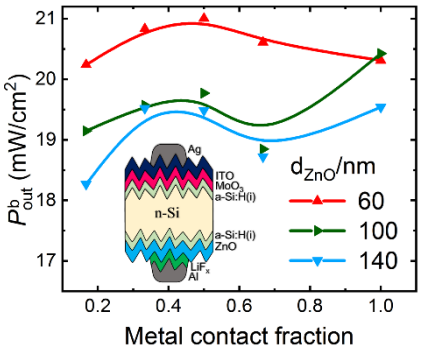

ToC figure

Full dopant-free bifacial silicon solar cells utilizing MoO_3/ITO/Ag hole contact and ZnO/LiF_x/Al electron contacts are demonstrated for the first time. The electron contacts feature full-area ZnO anti-reflective coating and LiF_x/Al finger contact, allowing bifacial application. The optimized cells with 60 nm ZnO and 50%-metal contact fraction achieve estimated output power density improvement of 0.7 mW/cm^2, compared with the monfacial reference cells.